Sb₂Se₃ Thin-Film Growth by Solution Atomic Layer Deposition

Vanessa M. Koch, Jaroslav Charvot, Yuanyuan Cao, Claudia Hartmann, Regan G. Wilks, Ivan Kundrata, Ignacio Mínguez-Bacho, Negar Gheshlaghi, Felix Hoga, Tobias Stubhan, Wiebke Alex, Daniel Pokorný, Ece Topraksal, Ana-Sunčana Smith, Christoph J. Brabec, Marcus Bär, Dirk M. Guldi, Maïssa K. S. Barr, Filip Bureš,* and Julien Bachmann*

ACCESS | 📊 Metrics & More | 📄 Article Recommendations | 🅢🅘 Supporting Information

ABSTRACT: We establish solution atomic layer deposition (sALD) for the controlled growth of pure Sb₂Se₃ thin films under mild conditions, namely, room temperature and atmospheric pressure. Upscaling this process yields Sb₂Se₃ thin films with high homogeneity over large-area (4″) substrates. Annealing of the initially amorphous material leads to highly crystalline and smooth Sb₂Se₃ thin films. Removing the constraints of thermal stability and sufficient volatility in sALD compared to traditional gas-phase ALD opens up a broad choice of precursors and allows us to examine a wide range of Se²⁻ precursors, of which some exhibit facile synthetic routes and allow us to tune their reactivity for optimal experimental ease of use. Moreover, we demonstrate that the solvent used in sALD represents an additional, attractive tool to influence and tailor the reactivity at the liquid−solid interface between the precursors and the surface.
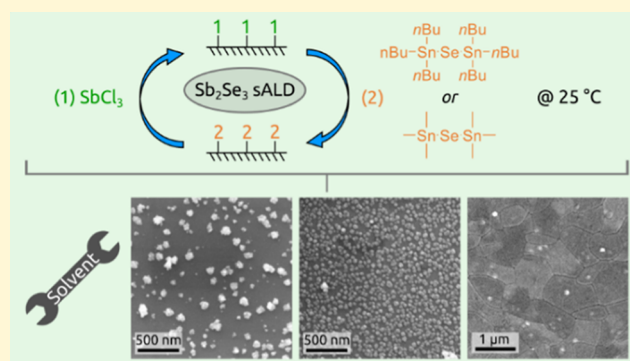
INTRODUCTION

Beyond its low toxicity, antimony selenide (Sb₂Se₃) features advantageous physical properties: its band gap of 1.17 eV is ideal to extract most of the solar spectrum, and its absorption coefficient >10⁵ cm⁻¹ over the full visible range allows it to be used as an ultrathin light absorber layer in solar cells (<100 nm in a planar configuration). These aspects have put it under increasing scrutiny as an alternative light-absorbing material.[1,2] To increase the power conversion efficiency of solar cells based on Sb₂Se₃ films, research has been dedicated mostly to three aspects: (1) engineering the Sb₂Se₃ interface to optimize the band alignment and passivate surface defects;[3] (2) achieving [001] preferential orientation of the crystal in order to minimize the electrical resistance along the transport direction;[4] and (3) improving the stoichiometry and homogeneity of the Sb₂Se₃ film. In particular, Se vacancies in Se-deficient films enhance recombination.[5,6] Therefore, special emphasis has to be placed on preparative methods allowing for perfect control of the stoichiometry. So far, most of the champion cells based on Sb₂Se₃ have been prepared by physical growth methods such as rapid thermal evaporation, vapor transport deposition, and closed-space sublimation (9.2%).[3,7,8] Chemical growth methods have been explored, as well, including electrodeposition, spin-coating, and atomic layer deposition (ALD).[9−11] Among these, ALD relies on complementary, self-limiting acid−base reactions between the solid surface and molecular precursors delivered from the gas phase. With specific precursors used at moderate

temperatures to deliver each ion, Sb(+III), on the one hand, and Se(−II), on the other hand, ALD promises to achieve not only outstanding thickness control (on including non-planar or nanostructured substrates) but also perfect stoichiometry.[11−13] However, the limited availability of reliable Se ALD precursors has impeded the development of Sb₂Se₃ ALD. For example, highly toxic and unstable H₂Se has been combined with the caustic SbCl₃ to generate corrosive HCl as a byproduct at 300 °C and a chlorine-contaminated film growing at 2.2 Å/cycle.[13] Bis(trimethylsilyl) selenide, Se(SiMe₃)₂, is the only established alternative to H₂Se which combines sufficient volatility with the necessary thermal stability and reactivity.[11] Selenium dimethyl-dithiocarbamate, Se(S₂CNMe₂)₄, has been proposed but yields a relatively slow growth of about 0.28 Å/cycle at 150 °C and exhibits a narrow ALD window.[12]

Here, we report a Sb₂Se₃ film deposition process by "solution ALD" (sALD). This novel method relies on the self-limiting surface chemistry principles of ALD but performs the reactions of the solid surface with precursors dissolved in an appropriate solvent as opposed to gaseous ones in traditional ALD. The
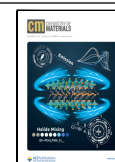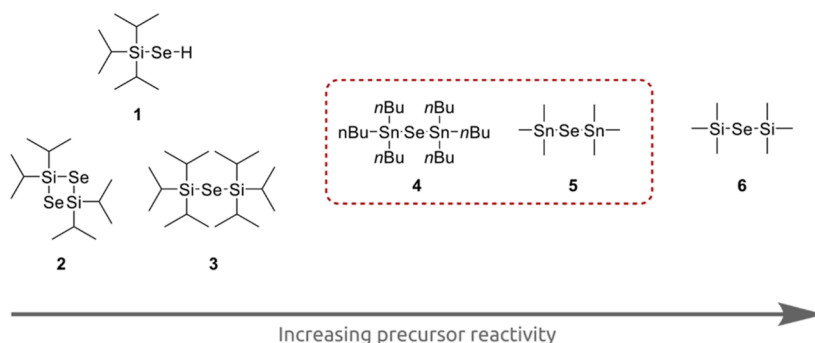
Figure 1. Molecular structures of Se precursors examined for the sALD of Sb_2Se_3.
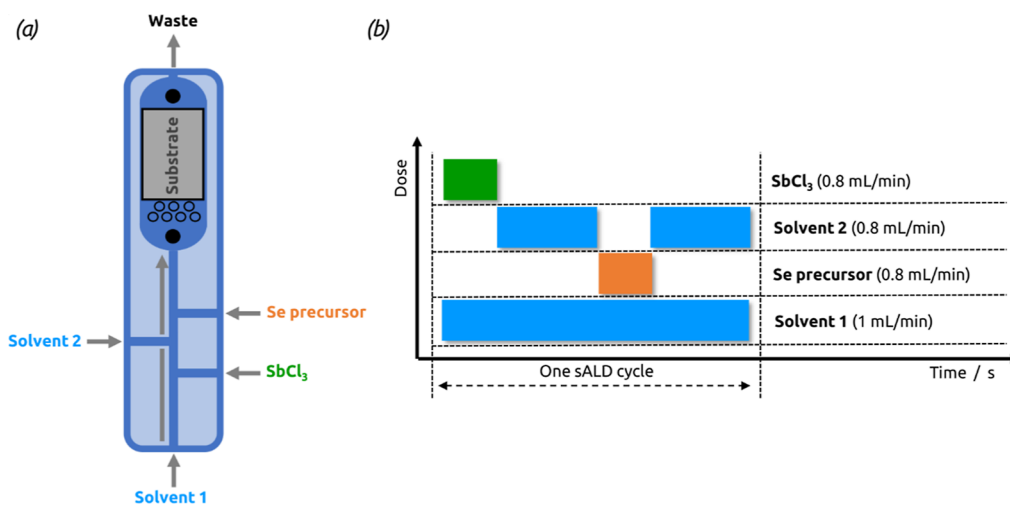

Figure 2. (a) Scheme of the research-scale sALD microfluidic reactor in which precursor flows are injected laterally into the continuous flow of carrier solvent. (b) Pulse and purge sequence of the two precursors and solvent with respective flow rates.

volatility requirement usually associated with ALD for the molecular precursors is thus eliminated, which opens up the range of potentially exploitable precursor chemistry significantly. In that vein, we have explored variants of the classic bis(trimethylsilyl)selenide precursor **6** with various reactivities (Figure 1).[14,15] Freedom from the volatility constraint allows synthetic chemists to place the emphasis on ease of handling and economical access, with silyl derivatives bearing bulky secondary substituents and with *n*-alkylstannyl selenides as novel alternatives, **1−5**.[14,15] All of them are readily soluble in various organic solvents, albeit not always volatile.

We have found that the least reactive compounds **1−3**[14,15] yield no appreciable deposition in sALD at room temperature, whereas the trimethylsilyl and trimethylstannyl derivatives **6** and **5** achieve similar deposition rates. The more encumbered *n*-tributylstannyl **4** bearing longer alkyl chains yields a slightly lower deposition rate. Based on this preliminary screening, we organize the following sALD study into three sections: we will first perform the full ALD demonstration in a small-scale reactor with compound **4**, which is the easiest to handle. The process and materials parameters obtained with **4** and **5** will be compared next. Finally, we perform a scale-up using **5**, which yields superior performance in terms of both process and materials quality.[16,17]

■ **EXPERIMENTAL SECTION**

Substrate Preparation. 30 nm thick amorphous TiO_2 thin films (TiO_2 target, 99.99%) were deposited on previously UV−ozone-cleaned (30 min) silicon wafers with native oxide (Si/SiO_2, Silicon Materials Inc.) by radio frequency (RF) magnetron sputtering (CRC 622 model, Torr International, Inc.) at a working pressure of 0.3 Pa with a power density of 2.5 W cm^{-2}. The deposition rate was 0.1 Å/s. The working gas (argon) was kept at a flow rate of 5 sccm. The base pressure was 1×10^{-4} Pa. The deposited TiO_2 films were annealed at 475 °C for 4 h in a muffle furnace in a N_2 atmosphere to result in anatase-phase TiO_2.

For the substrate study, a Si/SiO_2 wafer coated with sputtered TiO_2 was dipped overnight in a $ZnCl_2$ solution (0.5 wt % in MeOH). For the pretreatment with piranha solution, a Si/SiO_2 wafer was dipped for 10 min in freshly prepared piranha solution, rinsed afterward with deionized water, dried with a N_2 gun, and subsequently subjected to Sb_2Se_3 deposition. Sb_2S_3 was deposited *via* ALD onto Si/SiO_2 wafers as described in our previous work:[18,19] the precursors used are $Sb(NMe_2)_3$ (99.99%, Sigma-Aldrich) and H_2S (3% vol in N_2, Air Liquide). N_2 was used as the carrier gas. Pulse, exposure, and purge durations were set to 1.5, 15, and 15 s for $Sb(NMe_2)_3$, and 0.2, 15, and 15 s for H_2S, respectively. The Sb precursor was kept at 40 °C, and the chamber temperature was set to 120 °C for Sb_2S_3 depositions. Amorphous Sb_2S_3 is converted to the stibnite phase by annealing the samples on a hot plate in a N_2 glovebox at 300 °C for 30 min.

For TiO_2 nanotubes (TNTs) on Si/SiO_2 substrates, a previously reported procedure has been used:[20] namely, the substrates were UV−ozone-cleaned for 30 min with subsequent deposition of ~300 nm-thick Ti thin films from a Ti target (99.99%) by RF sputtering with a working pressure of 0.3 Pa, a power density of 3.3 W cm^{-2} and an argon flow of 5 sccm. The resulting deposition rate was 0.8 Å/s. The Ti thin films were anodized in a two-electrode setup in an ethylene glycol-based electrolyte containing 0.5% NH_4F, 3% H_2O, and 0.5 wt % H_3PO_4 (85%) at 60 V. After anodization, the samples were left in the electrolyte
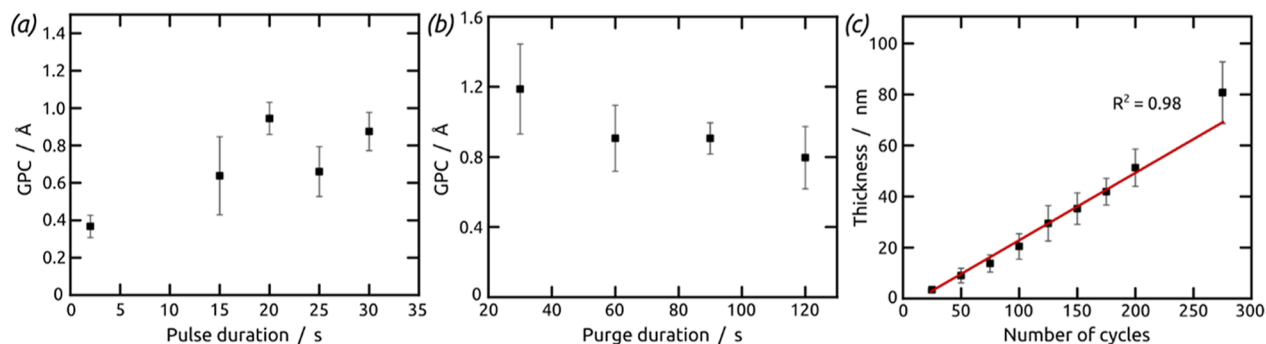
Figure 3. ALD growth mode demonstrated *via* parameter variation (precursors are delivered as 1 mM solutions in *n*-hexane). (a) Pulse duration investigation (purge kept at 90 s, 20 cycles). (b) Purge duration investigation (pulse kept at 20 s, 20 cycles). (c) Linear growth of the film on oxide-covered Si wafers (pulse 20 s, purge 120 s).
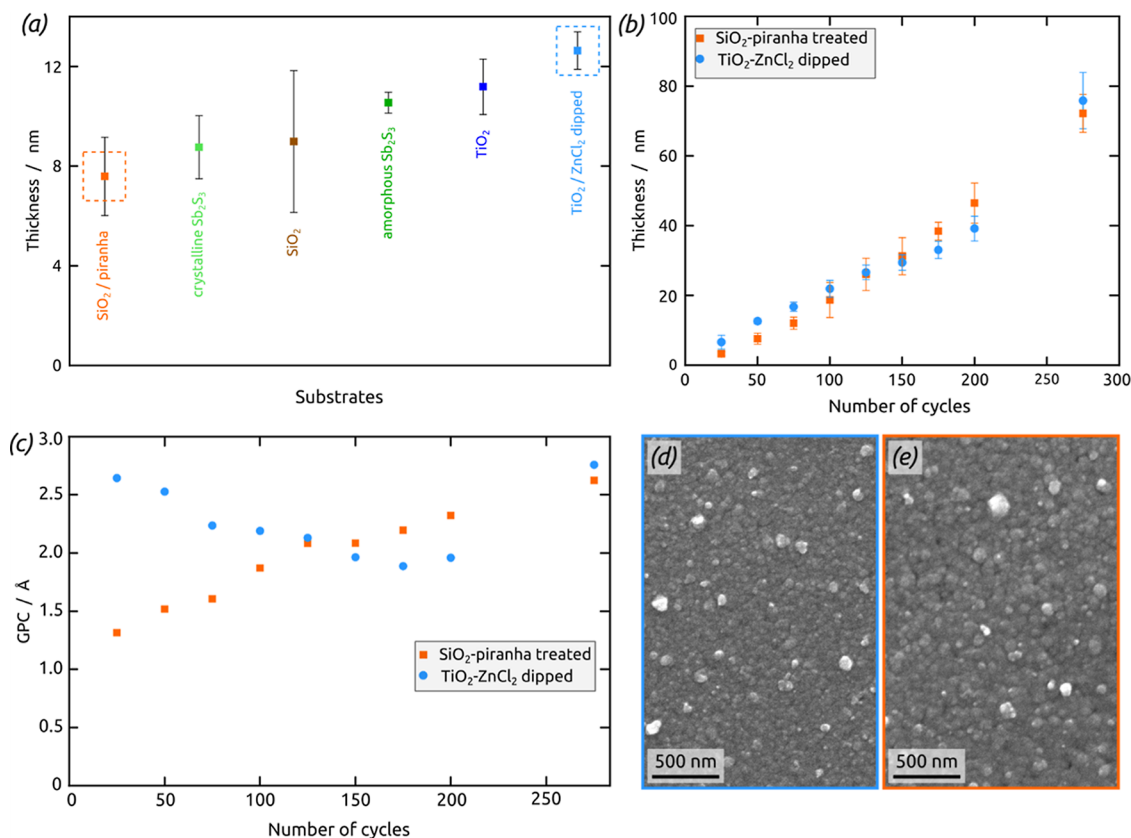

Figure 4. Influence of substrates on Sb_2Se_3 sALD. (a) Thickness of films after 50 cycles on six different substrates. (b) Full growth study on two selected substrates. (c) Apparent GPC values derived from (b), highlighting a nucleation effect. Scanning electron micrographs of Sb_2Se_3 films obtained after 275 sALD cycles on (d) a piranha-cleaned SiO_2 wafer and on (e) a $ZnCl_2$-dipped, TiO_2-coated wafer.

for 20 min without applied potential to widen the inner tube diameter. A subsequent rinse with ethanol and keeping the samples in an ethanol bath overnight was followed to remove the residual electrolyte. The samples were transferred to a deionized water bath for 2 h and afterward left to dry in air. The as-grown amorphous TNTs were annealed at 500 °C for 1 h on a hotplate in ambient atmosphere to result in crystalline anatase-phase TiO_2.

sALD on Research-Scale Setup. Sb_2Se_3 depositions were carried out in a custom sALD setup using a homemade stainless steel reaction chamber (Figures 2 and S1, Supporting Information), a peristaltic pump (Reglo ICC, four independent channels, from Ismatec, Cole-Parmer GmbH), flexible elastomeric tubings (Viton, Ismatec, Cole-Parmer GmbH), HPLC tube connectors (PEEK and PVDF, Cole-Parmer GmbH), and PTFE tubing (Bohlender GmbH) were used to transport the two precursors and the purge solvent from Schlenk flasks

(N_2). The flow rates were set to 0.8 mL/min for precursors and 1 mL/min for purging solvent. $SbCl_3$ (99.95%, Sigma-Aldrich GmbH) was used as an antimony source and compounds **1−6** (Figure 1) as a selenium source. Precursors were dissolved in *n*-hexane (≥99%, Honeywell Riedel-de Haën GmbH), which was freshly distilled over a Na/K alloy before use. The deposition was made, as an injection type, where one-solvent channel was running the whole time and 1 mM concentrated precursors were injected in (20 s pulse). Between every pulse, the second solvent channel was activated (120 s purge) for faster precursor removal.

sALD on Scaled-Up Setup Based on a Slot-Die Head. For upscaling Sb_2Se_3 sALD, a homebuilt sALD setup based on a modified slot-die coater was been used. The setup was stored under inert (N_2) conditions. A peristaltic pump (Reglo ICC, four independent channels, from Ismatec, Cole-Parmer GmbH), flexible elastomeric tubings
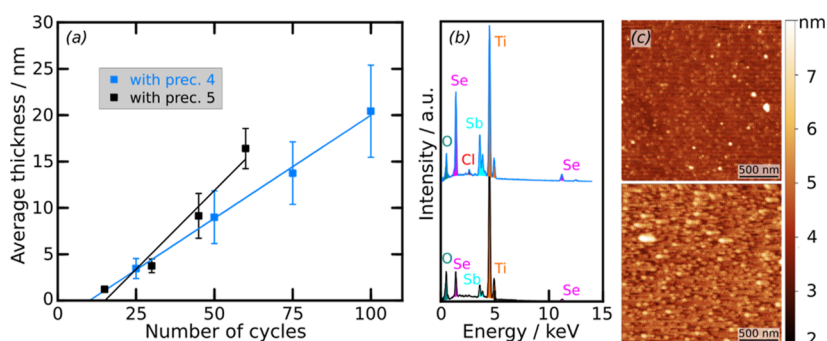
Figure 5. Reactivity of two distinct precursors. (a) sALD growth curves obtained with **4** and **5** as the Se source (pulse and purge durations: 15 and 120 s; concentrations: 1 mM, respectively). The more reactive precursor yields a faster growth. (b) EDX characterization of films obtained with 100 cycles Sb_2Se_3 on TiO_2 nanotubes (TNTs) with **4** (top, Se/Sb = 1.8) and **5** (bottom, Se/Sb = 1.8) as the Se precursor, respectively. The more reactive precursor eliminates Cl remnants from the solid. (c) AFM micrographs of Sb_2Se_3 deposits obtained on Si/SiO_2 wafers after 5 sALD cycles from **4** (top) and **5** (bottom) as Se source from *n*-hexane, respectively. The more reactive precursor delivers more homogeneous nucleation.
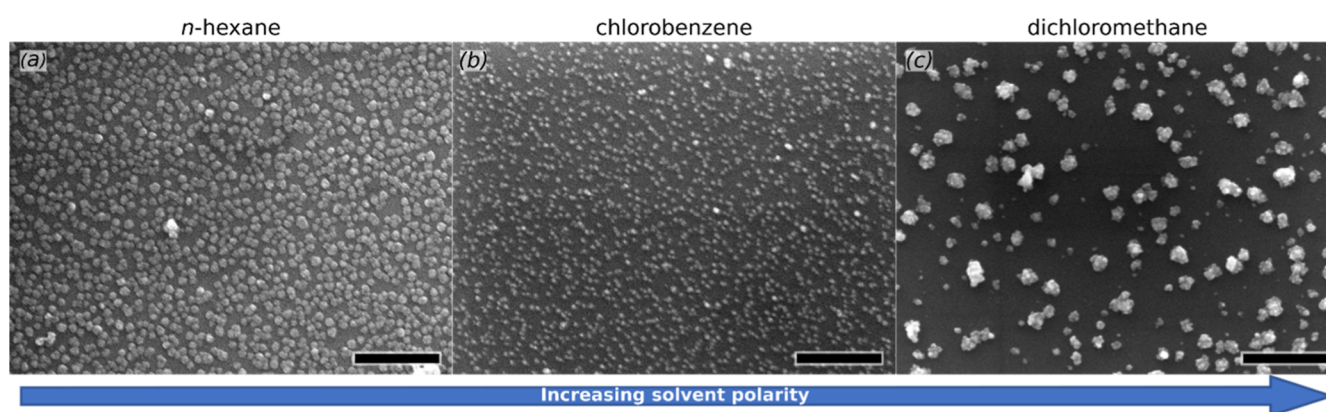

Figure 6. SEM micrographs of Sb_2Se_3 deposits after 50 cycles obtained by sALD on Si/SiO_2 substrates from 1 mM $SbCl_3$ and 1 mM of Se precursor **5** from (a) *n*-hexane, (b) chlorobenzene, and (c) dichloromethane as the solvent, respectively. The scale bar in each micrograph represents 500 nm.

(Viton, Ismatec, Cole-Parmer GmbH), HPLC tube connectors (PEEK and PVDF, Cole-Parmer GmbH), and PTFE tubing (Bohlender GmbH) were used to transport the two precursors and the purge solvent in a consecutive, cyclic manner from brown glass vials (stored under N_2) toward the slot-die head of the sALD setup and onto the substrates. The flowrates of the two precursor solutions and the purge solvent were set to 1.75 mL/min. $SbCl_3$ (≥99.95%, Sigma-Aldrich GmbH) as a Sb(III) source and bis-(trimethylstannyl)selenide (**5**) as a Se^{2-} source were used for the sALD of Sb_2Se_3. *n*-Octane (≥99%, Carl Roth GmbH & Co. KG) was used to dissolve the precursors with a concentration of 1 mM, respectively. Furthermore, *n*-octane was used as the purging solvent. The standard pulse and purge durations were set to 10 and 120 s, respectively.

Instrumental Methods. Spectroscopic ellipsometry measurements were performed using a SENPro spectroscopic ellipsometer (SENTECH Instruments GmbH). All measurements were conducted at an angle of 70° in a spectral range from 370 to 1050 nm. Data analysis was performed with the software SpectraRay 3.

Grazing-incidence X-ray diffraction (GI-XRD) was performed using a D8 DISCOVER X-ray diffractometer (Bruker Corporation) with a Cu K_α source (20 kV). The Crystallographic Open Database (COD) was used to assign the diffraction pattern of crystalline Sb_2Se_3 and TiO_2.

For the scanning electron microscopy (SEM) and energy dispersive X-ray spectroscopy (EDX) measurements, a JSM-F thermal field-emission scanning electron microscope (JEOL GmbH) with an acceleration voltage of 5 kV and a secondary electron detector was used. Additionally, a GeminiSEM 500 thermal field-emission scanning electron microscope (Carl Zeiss Microscopy GmbH) with an acceleration voltage of 2 kV and an in-lens detector was used for higher-resolution SEM micrographs. Images were analyzed with the self-developed protocol calling ImageJ[21] and Cell-pose[22] software.

The Sb_2Se_3 samples (vacuum-packed) were mailed from FAU to HZB and subsequently introduced into an Ar-purged glovebox directly attached to the (ultra-high vacuum) UHV-backbone of the Energy Materials *In Situ* Laboratory Berlin (EMIL). The X-ray photoelectron spectroscopy (XPS) measurements were performed employing a non-monochromatized PREVAC RS40B1 Mg K_α/Al$_\alpha$ twin anode X-ray source and a Scienta Omicron Argus CU electron analyzer. The samples were studied with a non-monochromatic Mg K_α source at a base pressure of the surface analysis system of <5 × 10^{-9} mbar. For the measurements of the survey spectrum, a pass energy of 100 eV was used, and a pass energy of 30 eV was used for the detailed spectra. The energy scale was calibrated using a clean Au foil, setting the Au 4f$_{7/2}$ line to the binding energy of 84.00 eV. Spectral intensities were normalized at the low-binding energy background, and a vertical offset is added for clarity.

3D maps of the lateral variation of the thickness were conducted by an EP4 imaging ellipsometer equipped with a DCC camera (Accurion GmbH). For the measurement of the whole wafer, single maps (2× objective, single wavelength) were stitched in order to map the full area. Mapping a line across the whole wafer was conducted with a 10× objective, single wavelength, and stitching of the recorded maps. The high-resolution map of an area of 228 × 285 μm^2 was recorded using a 50× objective and eight wavelengths. The wavelengths were: 384.9, 447.2, 522.7, 595.4, 657.7, and 840.6 nm. All imaging ellipsometry measurements were fitted using the EP4 model software and point-to-point fits were based on a Drude–Lorentz model for Sb_2Se_3.

Atomic force microscopy images are obtained with a Veeco Dimension 3100 microscope using the tapping mode. Silicon probe tips from Bruker were used with a spring constant of 2 N m^{-1} and a resonance frequency of 70 kHz. The resolution is 512 × 512 pixels for imaged surfaces of 2 × 2 μm^2. The digital image processing was performed with Gwyddion 2.53.
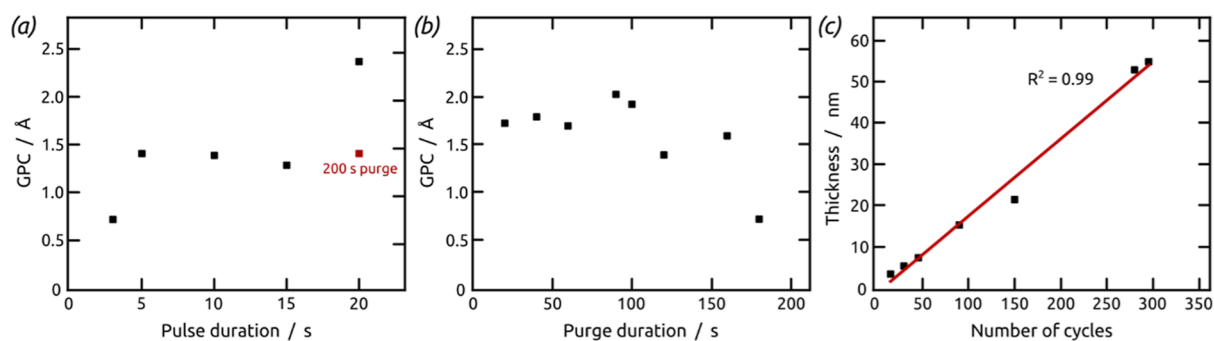
Figure 7. Demonstration of sALD growth mode after process scale-up to a slot-die coating head of 10 cm lateral size. (a) Self-limiting surface chemistry established by pulse duration investigation (purge maintained at 120 s except for one datapoint as marked). (b) Chemisorption behavior established by purge duration variation (pulse maintained at 10 s). (c) Linear growth curve (pulse 10 s, purge 120 s) determined on an Si/SiO$_2$ wafer coated with TiO$_2$ by RF sputtering. The concentration of each precursor is kept constant at 1 mM.

The optical UV−vis absorption spectra were measured with an UV−visspectrophotometer equipped with a DH-2000-L light source, a HR40000 spectrometer, and an ISP-50-8-R integrating sphere (Ocean Optics, Inc.).

Raman spectroscopy of the thin film was measured in ambient conditions on an alpha-R confocal Raman microscope in backscattering with a 532 nm excitation wavelength (WiTec Wissenschaftliche Instrumente und Technologie GmbH).

RESULTS AND DISCUSSION

sALD Growth Study. Our sALD study is performed on a research-scale sALD reactor (see Figure S1, Supporting
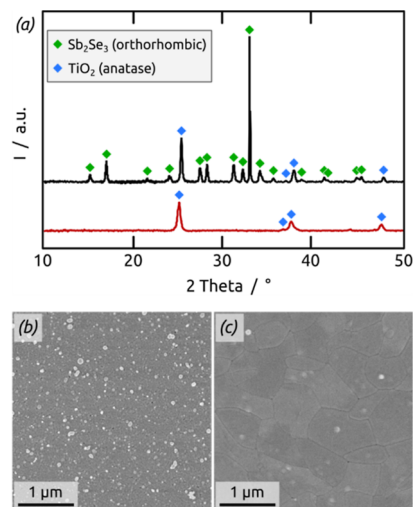

Figure 8. (a) GI-XRD diffractogram of a sample featuring 150 Sb$_2$Se$_3$ sALD cycles on TiO$_2$ nanotubes before (red curve) and after annealing at 300 °C for 5 min in N$_2$ atmosphere (black curve). Scanning electron micrographs of 350 cycles Sb$_2$Se$_3$ as grown (b) and annealed at 300 °C for 5 min under N$_2$ (c). Note: A Si/SiO$_2$ substrate has been used for SEM to minimize charging effects during the measurement.

Information) of a design improved from the previously reported one.[23] The first precursor (SbCl$_3$), solvent, and the second precursor ([n-Bu$_3$Sn]$_2$Se, **4**) are introduced into the microfluidic reaction chamber in an alternating manner by coordinated peristaltic pumps turned on and off in order to define the alternating surface reactions with both precursors (Figure 2). Care is taken to avoid direct reaction of both precursors with each other in the solution, which would yield uncontrolled "chemical bath deposition" (CBD, the liquid-phase equivalent
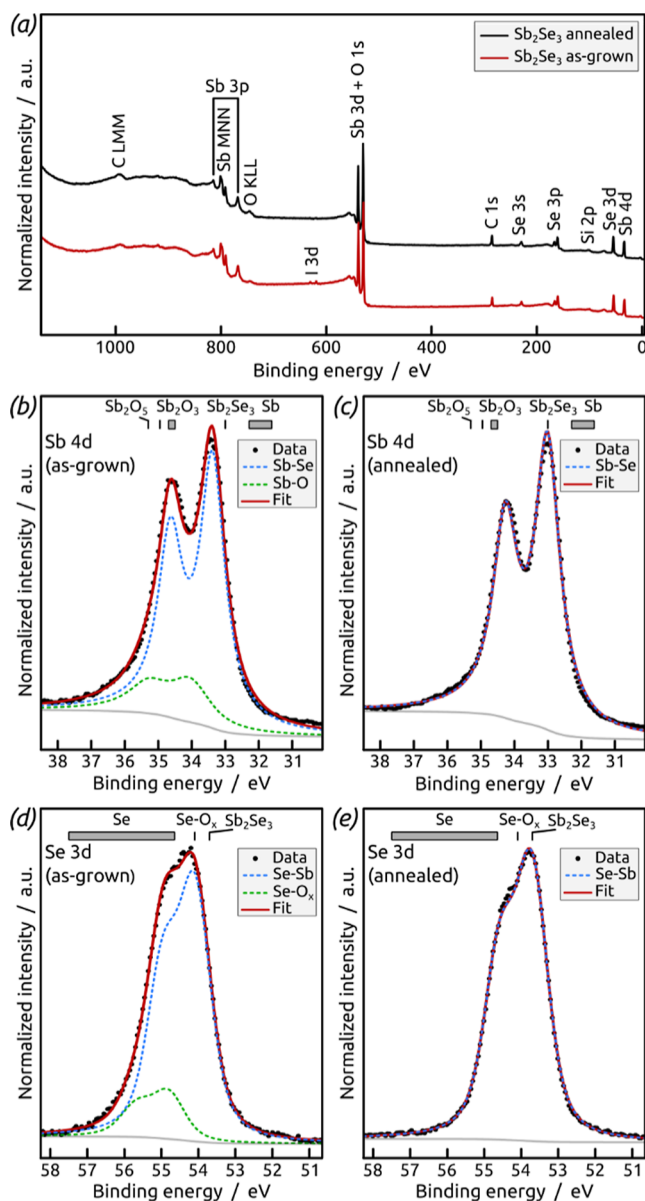

Figure 9. XPS of 300 cycles of Sb$_2$Se$_3$ on a native Si wafer. (a) Survey spectrum, (b) Sb 4d core level spectrum of as-grown Sb$_2$Se$_3$, (c) Sb 4d core level spectrum of annealed Sb$_2$Se$_3$, (d) Se 3d core level spectrum of as-grown Sb$_2$Se$_3$, (e) Se 3d core level spectrum of annealed Sb$_2$Se$_3$.
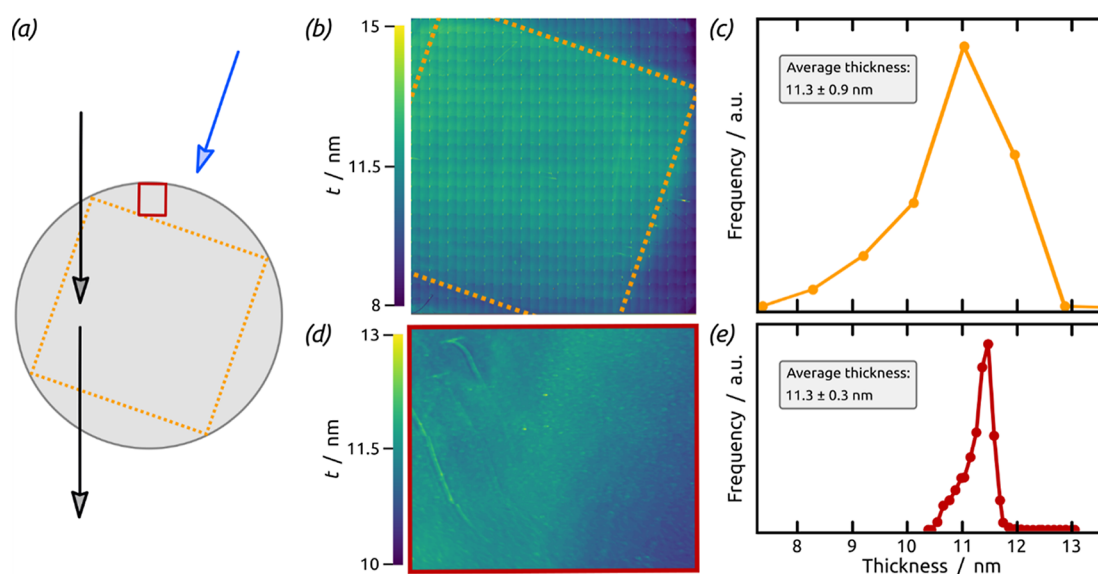
Figure 10. Imaging ellipsometry of a native oxide Si wafer coated with 80 cycles of Sb_2Se_3. (a) Scheme of the coated wafer indicating the direction of flow during sALD (blue arrow) and the optical axis during the ellipsometry measurement (black arrows) with mapped areas (orange, red). (b) Ellipsometry map over the full wafer (7.2×7.0 cm^2) ($2\times$ objective, single wavelength, stitched maps). Note: the slightly higher thickness within the orange dashed square can be explained by the flow behavior in the sALD setup. (c) Film thickness distribution determined over the area of the full wafer. (d) High-resolution ellipsometry map (228×285 μm^2) ($50\times$ objective, eight wavelengths). (e) Film thickness distribution determined within the red-marked area on the wafer.

to chemical vapor deposition).[24] The substrates are pieces of silicon wafer with thermal oxide and their thicknesses are determined by spectroscopic ellipsometry.

Figure 3a shows the saturation behavior of the sALD reactions at room temperature when the dosage of both precursors (1 mM in n-hexane) is varied: the growth per cycle (GPC) reaches a plateau at 15 to 20 s pulse durations. With 20 s taken as the standard pulse duration, the influence of the purge and the transition from CBD to sALD growth mode is demonstrated in Figure 3b. Under standard conditions, Figure 3c reveals the linear dependence of the film thickness on the number of ALD cycles performed. A stable GPC of 2.1 Å is achieved from pulse and purge duration of 20 and 120 s, respectively.

The chemical nature of ALD and the inherently poor adhesion between oxides and heavier chalcogenides lead one to expect that nucleation may depend on the substrate chosen. We compare thermal SiO_2-covered Si wafers, piranha-cleaned SiO_2, TiO_2-coated substrates, $ZnCl_2$-dipped TiO_2 surfaces, amorphous Sb_2S_3 (ALD-deposited), and crystalline Sb_2S_3 (after annealing) in Figure 4a. This list of substrates represents a variety of chemical reactivities: classical oxides on standard Si wafer substrates (SiO_2), after standard surface cleaning to remove any organic residues (piranha clean) and for photovoltaic applications (TiO_2), oxide activated according to a published procedure to add some surface metal-chloride moieties ($ZnCl_2$ treatment),[25,26] and sulfide surfaces providing typically better adhesion with heavier chalcogenides than oxides (Sb_2S_3). Indeed, the apparent growth rate (calculated from the thickness determined after 50 sALD cycles) varies, Sb_2Se_3 growing not only fastest but also most reproducibly on the TiO_2 (with or without $ZnCl_2$ dip) and amorphous Sb_2S_3 layers. A more complete comparison of the extreme substrates (Figure 4b,c) reveals that the difference is most pronounced in the initial stages of deposition, indicating that nucleation (as opposed to growth) causes the disparities. This could be due to the formation of $-O-ZnCl$ units in place of the $-OH$ groups

originally present at the surface, which generates a larger driving force for reaction with $(R_3Sn)_2Se$ in the initial ALD cycles (*via* the formation of R_3Sn-Cl). This observation is also in line with characteristics expected of ALD-type growth. We note that similar nucleation delays affected by surface treatments have been observed in classical, gas-phase ALD, most prominently for the ALD of metals on oxides.[25] Scanning electron micrographs of rather thick films (275 cycles, Figure 4d,e) confirm that the morphology of the solid is not significantly distinct.

Effect of Precursors. Let us now investigate how increasing the precursor reactivity by moving from **4** to **5** will affect the growth and material parameters. Figure 5a compares deposits obtained from the two different bis(trialkylstannyl)selenides $(R_3Sn)_2Se$ (R = n-butyl for **4** and R = methyl for **5**) using the process parameters defined above. The more reactive **5** also delivers a linear ALD type of growth with a seemingly similar nucleation delay when compared with **4** but with a slightly higher thickness GPC value of 2.6 Å. What may appear to represent a slight difference in nucleation delay between **4** and **5** is within measurement error on the curves of Figure 5a. In fact, a more accurate investigation by AFM taken after 5 cycles of Sb_2Se_3 sALD confirms that nucleation is definitely not faster with **4**. Indeed, the AFM micrographs on Si/SiO_2 substrates (Figure 5c) show that in the initial stages of deposition, the less reactive selenide precursor **4** generates individual particles separated by significant distances, whereas its more reactive counterpart **5** gives rise to much more homogeneous nucleation. The quantification of surface coverage highlights this, with 14 and 3% obtained with **4** and **5**, respectively (based on AFM phase contrast, see Supporting Information for more details).

The quantitative advantages observed in nucleation and growth are complemented by a much more significant, qualitative, improvement of the purity. Indeed, EDX measurements of the chemical composition of deposits obtained on substrates of large surface area [100 cycles on titania nanotubes (TNTs), Figure 5b] reveal many similarities and a distinct

difference. First, the expected signals for elements Sb, Se, Ti, and O deliver a Se/Sb ratio slightly larger than the stoichiometric value of 1.5 in both cases, which might be beneficial for application in thin film solar cells as Se deficiency is often reported to be detrimental.[6] Second, one observes that the less reactive butyl precursor **4** allows for the undesired incorporation of chloride ligands from the Sb precursor. This is not the case with precursor **5**, which achieves a complete reaction with $SbCl_3$ and prevents the appearance of residual Cl in the solid (within the detection limit on the order of 0.8%, to be confirmed by XPS later). In summary, we have several good reasons to focus on precursor **5** for the remainder of our study.

Effect of Solvents. The reactivity and selectivity of molecular reagents are also influenced by their environment. In sALD, solvents and additives can not only interact with the molecules that react with the surface but also with the solid surface itself. This fact is in stark contrast with classical ALD methodology, where such fine-tuning of the chemical environment is not possible. Within the solubility constraints, three different solvents were chosen to investigate this effect on our Sb_2Se_3 sALD process, namely, *n*-hexane, chlorobenzene, and dichloromethane (on Si/SiO_2 substrates). The SE micrographs in Figure 6 present the contrasting results obtained after 50 cycles of Sb_2Se_3 sALD: it demonstrates convincingly a strong influence of solvent polarity on nucleation density and thereby on surface coverage. In essence, polar solvents seem to inhibit the reactivity of either the precursor(s) or the surface. The detailed SE micrograph analysis presented in the Supporting Information (Figure S5) confirms in quantitative terms a decreasing surface coverage as the solvent polarity increases, confirming a decrease in reactivity. However, the size distribution of the crystallites does not follow a monotonic trend. The reduction in average size observed first (from hexane to chlorobenzene) is further in line with the reduced nucleation chance per cycle just described, but the subsequent increase in particle size (from chlorobenzene to dichloromethane) seems to be in contradiction with it. A possible interpretation of it is provided by the surface mobility of adsorbates.

Process Scale-Up. The results presented so far have demonstrated the self-limiting ALD growth behavior of the $(R_3Sn)_2Se + SbCl_3$ deposition procedure and have established the methyl derivative **5** in *n*-hexane to deliver the best properties. To prove the versatility of the sALD technique and take a first step toward large-scale manufacturing of Sb_2Se_3 thin films (for photovoltaic devices), we will now demonstrate how the Sb_2Se_3 sALD process can be scaled up on a modified slot-die setup with the capability to coat a whole 100 mm (4″) diameter wafer or substrates of up to 100 cm² area. In order to improve compatibility with regulations on volatile organic compounds (such as the EUs directive "on industrial emissions, integrated pollution prevention and control"),[27] we will replace *n*-hexane with *n*-octane, which provides essentially identical chemical profile with reduced vapor pressure. We will use as the standard substrates either TiO_2 (sputter-coated in RF mode on native oxide Si wafers) due to its advantageous nucleation behavior described above and its relevance to photovoltaic and photoelectrochemical devices, wherever possible, or a Si wafer piece (with thin native oxide) when necessary for the purpose of specific measurements. The data presented in Figure 7 demonstrate that the setup with slot-die coating head delivers sALD growth as well. The self-limiting behavior of the surface reactions is established in Figure 7a. It is slightly less ideal than the microfluidic setup in the sense that extremely long pulse

durations must be accompanied by increased purge durations as well. In the same vein, the purge behavior (Figure 7b) deviates from the desirable horizontal line somewhat. However, both graphs establish the presence of a quite large processing window over which parameter variations do not affect growth. In Figure 7c, the linear growth is seen to occur at a rate of 1.6 Å/cycle, a value compatible to that observed in the small microfluidic sALD setup.

Sb_2Se_3 Material Characterization. Detailed characterization of as-grown and annealed Sb_2Se_3 thin films was carried out in terms of crystallinity, morphology, and chemical composition by GI-XRD, SEM, EDX, XPS, and Raman spectroscopy. On TiO_2 nanotubes, grown by anodization[20] and used as a substrate to increase the absolute amount of deposit *via* increased specific surface area, the as-deposited material obtained after 150 sALD cycles is shown to be amorphous by GI-XRD (Figure 8a, red curve). After annealing the sample at 300 °C for 5 min in N_2 atmosphere, well-defined signals appear for crystalline, orthorhombic Sb_2Se_3 aligned with the reported pattern (COD 9007437), in addition to the signals of anatase-TiO_2 (COD 1526931) (Figure 8b, black curve).

The annealing also has a significant effect on the film morphology (Figure 8c). Indeed, the originally continuous but granular layer (after 350 sALD cycles of Sb_2Se_3 sALD) smoothens to generate very large and densely packed grains, with individual crystals in the size range of up to 1 *μ*m laterally (whereas they are only 60 nm thick). A small density of distinct pinholes is still present at this film thickness. Finally, annealing also extends the film's light absorption into the near infrared (Figure S2 in the Supporting Information) and sharpens its characteristic Raman peak near 200 cm^{-1} (Figure S3).

The chemical composition of sALD Sb_2Se_3 films on planar substrates as determined by EDX contains the elements Sb and Se in a ratio of approximately 1:1, which deviates significantly from the theoretical value of 2:3 and suggests a Se deficiency in the films. This is in contradiction with the numbers obtained on structured substrates of high specific surface area (presented above). It may not be representative of the film after preparation, as it could be caused by superficial aerobic oxidation, which influences the overall composition of ultrathin films sensitively, or by potential degassing of volatile Se in the high vacuum conditions of the SEM. Further insight is delivered by XPS for films (300 cycles Sb_2Se_3 on Si substrates with thin native oxide to avoid electrostatic charging) before and after annealing (300 °C, 5 min, N_2). The signals expected for Sb and Se are found, whereas the absence of Sn and Cl proves the purity of the Sb_2Se_3 films (Figures 9a and S6, Supporting Information). The Sb 4d region exhibits defined spin—orbit components for Sb $4d_{5/2}$ and Sb $4d_{3/2}$. The main contributions at 33.4 and 34.6 eV can be attributed to Sb in a Se environment, consistent with Sb_2Se_3.[28] A small contribution of oxide-bound Sb is found at 34.1 and 35.3 eV, which we attribute to surface oxidation to Sb_2O_3 (Figure 9b).[29] This contribution disappears upon annealing (Figure 9c). The Se 3d core-level spectra before and after annealing confirm these results. The main contribution within the spin—orbit pair Se $3d_{5/2}$ (54.2 eV)/Se $3d_{3/2}$ (54.8 eV) originates from Se bound to Sb (Figure 9d).[28] The fit reveals a minor amount of oxidation at 54.9 and 55.7 eV, stemming from a Se—O_x species, which completely disappears after annealing (Figure 9e). From XPS, the Sb/Se ratio is determined to be approximately 1:1. This is in agreement with the EDX results and confirms a Se deficiency in the Sb_2Se_3 films, hypothetically from the high-vacuum conditions under the X-ray beam. To sum up, the EDX and

XPS data provide evidence for the sALD growth of films which in the amorphous as-grown state are affected by superficial oxidation, whereas annealing to the crystalline state stabilizes a single-phase antimony selenide state.

Let us conclude by demonstrating the homogeneity of sALD deposits on the full wafer scale. Figure S7 in the Supporting Information and Figure 10 provide a characterization of thickness homogeneity over two different length scales is quantified by ellipsometric characterization. An imaging ellipsometry map recorded over an area of $228 \times 285 \ \mu m^2$ concurs with a line taken across the wafer diameter to exhibit a thickness variation of 3% (Figure S7, Supporting Information), whereas imaging over the full wafer ($7.2 \times 7.0 \ cm^2$) yields an inhomogeneity of 8% (Figure 10).

CONCLUSIONS

The ALD chemistry of heavier chalcogenides has been enabled by the seminal introduction of bis(trimethylsilyl)selenide and the corresponding telluride in 2009 but has not developed further (in terms of chalcogenide precursors) since then.[30] The constraints of (a) thermal stability, (b) sufficient acid−base reactivity, and (c) proper volatility, which must all be fulfilled simultaneously in classical ALD from the gas phase, have not enabled the group of precursors to be expanded beyond $(Me_3Si)_2E$, E = Se, Te, apart from isolated recent forays.[14,15] Removing the constraints (a) and (c) to a large extent in sALD has allowed us to investigate a broader range of $(R_3M)_2Se$ and related compounds, where R = Me, i-Pr, n-Bu; M = Si, Sn. Among this group, some representatives provide much facilitated synthetic access and the possibility to tune the reactivity for optimal experimental ease of use. sALD allows one to generate Sb_2Se_3 thin films in a controllable manner under mild conditions, namely, room temperature and atmospheric pressure. The process established here yields pure material in thin films of homogeneous thickness over large substrates and in the form of large crystals after annealing. This promising semiconductor is now available to use in a variety of applications.

An attractive aspect demonstrated in this study is the possibility of exploiting the solvent as a tool to influence and adjust the reactivity of molecular precursor and solid surface to each other. Here, we have found that the density of nucleation sites depends on the polarity of the solvent. Most likely, more polar solvents stabilize reactive surface groups more efficiently and inhibit reactions with the precursors. This is of importance for area-selective deposition, where the selectivity of the precursors must be tailored in order to deliver growth on a specific chemical functionality and no growth on another. We are convinced that solvents or even further additives will enjoy increasing importance in order to tune reactivity into this desirable window.

ASSOCIATED CONTENT

Ⓢ Supporting Information

The Supporting Information is available free of charge at https://pubs.acs.org/doi/10.1021/acs.chemmater.2c01550.

> Photo of the research-scale sALD reactor, UV−vis spectra, Raman spectra, SEM and EDX data, detailed SE micrograph image analysis, and additional XPS and imaging ellipsometry data (PDF)

AUTHOR INFORMATION

Corresponding Authors

Filip Bureš − *Institute of Organic Chemistry and Technology, Faculty of Chemical Technology, University of Pardubice, Pardubice 53210, Czech Republic;* ◉ orcid.org/0000-0002-2832-6673; Email: filip.bures@upce.cz

Julien Bachmann − *Chemistry of Thin Film Materials (CTFM), Interdisciplinary Center for Nanostructured Films (IZNF), Friedrich-Alexander Universität Erlangen-Nürnberg (FAU), Erlangen 91058, Germany;* ◉ orcid.org/0000-0001-6480-6212; Email: julien.bachmann@fau.de

Authors

Vanessa M. Koch − *Chemistry of Thin Film Materials (CTFM), Interdisciplinary Center for Nanostructured Films (IZNF), Friedrich-Alexander Universität Erlangen-Nürnberg (FAU), Erlangen 91058, Germany;* ◉ orcid.org/0000-0003-4560-787X

Jaroslav Charvot − *Chemistry of Thin Film Materials (CTFM), Interdisciplinary Center for Nanostructured Films (IZNF), Friedrich-Alexander Universität Erlangen-Nürnberg (FAU), Erlangen 91058, Germany; Institute of Organic Chemistry and Technology, Faculty of Chemical Technology, University of Pardubice, Pardubice 53210, Czech Republic*

Yuanyuan Cao − *Chemistry of Thin Film Materials (CTFM), Interdisciplinary Center for Nanostructured Films (IZNF), Friedrich-Alexander Universität Erlangen-Nürnberg (FAU), Erlangen 91058, Germany*

Claudia Hartmann − *Department Interface Design, Helmholtz-Zentrum Berlin für Materialien und Energie GmbH (HZB), Berlin 12489, Germany;* ◉ orcid.org/0000-0002-8017-8161

Regan G. Wilks − *Department Interface Design, Helmholtz-Zentrum Berlin für Materialien und Energie GmbH (HZB), Berlin 12489, Germany; Energy Materials In Situ Laboratory Berlin (EMIL), Helmholtz-Zentrum Berlin für Materialien und Energie GmbH, Berlin 12489, Germany;* ◉ orcid.org/0000-0001-5822-8399

Ivan Kundrata − *Chemistry of Thin Film Materials (CTFM), Interdisciplinary Center for Nanostructured Films (IZNF), Friedrich-Alexander Universität Erlangen-Nürnberg (FAU), Erlangen 91058, Germany; ATLANT 3D Nanosystems ApS, Kongens Lyngby 2800, Denmark*

Ignacio Mínguez-Bacho − *Chemistry of Thin Film Materials (CTFM), Interdisciplinary Center for Nanostructured Films (IZNF), Friedrich-Alexander Universität Erlangen-Nürnberg (FAU), Erlangen 91058, Germany;* ◉ orcid.org/0000-0003-1680-1729

Negar Gheshlaghi − *Chemistry of Thin Film Materials (CTFM), Interdisciplinary Center for Nanostructured Films (IZNF), Friedrich-Alexander Universität Erlangen-Nürnberg (FAU), Erlangen 91058, Germany*

Felix Hoga − *Automatic Research GmbH, Nürnberg 90403, Germany*

Tobias Stubhan − *Automatic Research GmbH, Nürnberg 90403, Germany*

Wiebke Alex − *Department of Chemistry and Pharmacy, Interdisciplinary Center for Molecular Materials (ICMM), Friedrich-Alexander University Erlangen-Nürnberg, Erlangen 91058, Germany*

Daniel Pokorný − *Institute of Organic Chemistry and Technology, Faculty of Chemical Technology, University of Pardubice, Pardubice 53210, Czech Republic*

Ece Topraksal − *PULS Group, Physics Department, Interdisciplinary Center for Nanostructured Films (IZNF), Friedrich-Alexander-Universität Erlangen-Nürnberg, Erlangen 91058, Germany*

Ana-Sunčana Smith − *PULS Group, Physics Department, Interdisciplinary Center for Nanostructured Films (IZNF), Friedrich-Alexander-Universität Erlangen-Nürnberg, Erlangen 91058, Germany; Group for Computational Life Sciences, Department of Physical Chemistry, Ruđer Bošković Institute, Zagreb 10000, Croatia*

Christoph J. Brabec − *Institute Materials for Electronics and Energy Technology (i-MEET), Friedrich-Alexander Universität Erlangen-Nürnberg (FAU), Erlangen 91058, Germany; Helmholtz-Institute Erlangen-Nürnberg for Renewable Energy (HI-ERN), Berlin 12489, Germany*

Marcus Bär − *Department Interface Design, Helmholtz-Zentrum Berlin für Materialien und Energie GmbH (HZB), Berlin 12489, Germany; Energy Materials In Situ Laboratory Berlin (EMIL), Helmholtz-Zentrum Berlin für Materialien und Energie GmbH, Berlin 12489, Germany; Helmholtz-Institute Erlangen-Nürnberg for Renewable Energy (HI-ERN), Berlin 12489, Germany; Department of Chemistry and Pharmacy, Friedrich-Alexander-Universität Erlangen-Nürnberg (FAU), Erlangen 91058, Germany;* orcid.org/0000-0001-8581-0691

Dirk M. Guldi − *Department of Chemistry and Pharmacy, Interdisciplinary Center for Molecular Materials (ICMM), Friedrich-Alexander University Erlangen-Nürnberg, Erlangen 91058, Germany;* orcid.org/0000-0002-3960-1765

Maïssa K. S. Barr − *Chemistry of Thin Film Materials (CTFM), Interdisciplinary Center for Nanostructured Films (IZNF), Friedrich-Alexander Universität Erlangen-Nürnberg (FAU), Erlangen 91058, Germany;* orcid.org/0000-0003-1587-2269

Complete contact information is available at:
https://pubs.acs.org/10.1021/acs.chemmater.2c01550

Author Contributions

The manuscript was written through contributions of all authors. V.M.K. and J.C. contributed equally to this work by performing the synthesis, the deposition, and most characterization. Y.C., I.M.-B., and N.G. performed SEM and AFM characterization, C.H. and R.G.W. performed XPS measurements and the analysis, I.K. performed the imaging ellipsometry characterization, W.A. performed the Raman characterization, F.H. and T.S. developed and built the slot-die setup and E.T. analyzed the SEM micrographs. V.M.K., Y.C., M.K.S.B., and J.B. finalized the manuscript. All authors proof-read the publication and have given approval to the final version of the manuscript.

Notes

The authors declare no competing financial interest.

■ ABBREVIATIONS

Sb_2Se_3, antimony selenide; PCE, power conversion efficiency; RTE, rapid thermal evaporation; VTD, vapor transport deposition; CSS, closed-space sublimation; ALD, atomic layer deposition; $Se(SiMe_3)_2$, bis(trimethylsilyl)selenide; $Se(S_2CNMe_2)_4$, selenium dimethyldithiocarbamate; sALD, solution ALD; CBD, chemical bath deposition; CVD, chemical vapor deposition; GPC, growth per cycle; EDX, energy-dispersive X-ray spectroscopy; TNTs, titania nanotubes; AFM, atomic force microscopy; SEM, scanning electron microscopy; GI-XRD, grazing incidence X-ray diffraction

■ REFERENCES

(1) Mavlonov, A.; Razykov, T.; Raziq, F.; Gan, J.; Chantana, J.; Kawano, Y.; Nishimura, T.; Wei, H.; Zakutayev, A.; Minemoto, T.; Zu, X.; Li, S.; Qiao, L. A review of Sb_2Se_3 photovoltaic absorber materials and thin-film solar cells. *Sol. Energy* **2020**, *201*, 227−246.

(2) Yang, W.; Zhang, X.; Tilley, S. D. Emerging Binary Chalcogenide Light Absorbers: Material Specific Promises and Challenges. *Chem. Mater.* **2021**, *33*, 3467−3489.

(3) Li, Z. Q.; Liang, X. Y.; Li, G.; Liu, H. X.; Zhang, H. Y.; Guo, J. X.; Chen, J. W.; Shen, K.; San, X. Y.; Yu, W.; Schropp, R. E. I; Mai, Y. H. 9.2%-efficient core-shell structured antimony selenide nanorod array solar cells. *Nat. Commun.* **2019**, *10*, 125.

(4) Krautmann, R.; Spalatu, N.; Gunder, R.; Abou-Ras, D.; Unold, T.; Schorr, S.; Krunks, M.; Oja Acik, I. Analysis of grain orientation and defects in Sb_2Se_3 solar cells fabricated by close-spaced sublimation. *Sol. Energy* **2021**, *225*, 494−500.

(5) Vidal-Fuentes, P.; Placidi, M.; Sánchez, Y.; Becerril-Romero, I.; Andrade-Arvizu, J.; Jehl, Z.; Pérez-Rodríguez, A.; Izquierdo-Roca, V.; Saucedo, E. Efficient Se-Rich Sb_2Se_3/CdS Planar Heterojunction Solar Cells by Sequential Processing: Control and Influence of Se Content. *Sol. RRL* **2020**, *4*, 2070075.

(6) Huang, M.; Cai, Z.; Wang, S.; Gong, X.-G.; Wei, S.-H.; Chen, S. More Se Vacancies in Sb_2Se_3 under Se-Rich Conditions: An Abnormal Behavior Induced by Defect-Correlation in Compensated Compound Semiconductors. *Small* **2021**, *17*, 2102429.

(7) Zhou, Y.; Wang, L.; Chen, S. Y.; Qin, S. K.; Liu, X. S.; Chen, J.; Xue, D. J.; Luo, M.; Cao, Y. Z.; Cheng, Y. B.; Sargent, E. H.; Tang, J. Thin-film Sb_2Se_3 photovoltaics with oriented one-dimensional ribbons and benign grain boundaries. *Nat. Photonics* **2015**, *9*, 409.

(8) Wen, X.; Chen, C.; Lu, S.; Li, K.; Kondrotas, R.; Zhao, Y.; Chen, W.; Gao, L.; Wang, C.; Zhang, J.; Niu, G.; Tang, J. Vapor transport deposition of antimony selenide thin film solar cells with 7.6% efficiency. *Nat. Commun.* **2018**, *9*, 2179.

(9) Wang, X. M.; Tang, R. F.; Yin, Y. W.; Ju, H. X.; Li, S. A.; Zhu, C. F.; Chen, T. Interfacial engineering for high efficiency solution processed Sb_2Se_3 solar cells. *Sol. Energy Mater. Sol. Cells* **2019**, *189*, 5−10.

(10) Ngo, T. T.; Chavhan, S.; Kosta, I.; Miguel, O.; Grande, H. J.; Tena-Zaera, R. Electrodeposition of Antimony Selenide Thin Films and Application in Semiconductor Sensitized Solar Cells. *ACS Appl. Mater. Interfaces* **2014**, *6*, 2836−2841.

(11) Yoo, S.; Yoo, C.; Park, E.-S.; Kim, W.; Lee, Y. K.; Hwang, C. S. Chemical interactions in the atomic layer deposition of Ge−Sb−Se−Te films and their ovonic threshold switching behavior. *J. Mater. Chem. C* **2018**, *6*, 5025−5032.

(12) Mahuli, N.; Halder, D.; Paul, A.; Sarkar, S. K. Atomic Layer Deposition of an Sb_2Se_3 Photoabsorber Layer Using Selenium Dimethyldithiocarbamate as a New Se Precursor. *Chem. Mater.* **2019**, *31*, 7434−7442.

(13) Browning, R.; Kuperman, N.; Moon, B.; Solanki, R. Atomic Layer Growth of InSe and Sb_2Se_3 Layered Semiconductors and Their Heterostructure. *Electronics* **2017**, *6*, 27.

(14) Charvot, J.; Pokorný, D.; Klikar, M.; Jelínková, V.; Bureš, F. Towards Volatile Organoselenium Compounds with Cost-Effective Synthesis. *Molecules* **2020**, *25*, 5212.

(15) Charvot, J.; Zazpe, R.; Macak, J. M.; Bureš, F. Organoselenium Precursors for Atomic Layer Deposition. *ACS Omega* **2021**, *6*, 6554−6558.

(16) Zazpe, R.; Charvot, J.; Krumpolec, R.; Hromádko, L.; Pavliňák, D.; Dvorak, F.; Knotek, P.; Michalicka, J.; Přikryl, J.; Ng, S.; Jelínková,

V.; Bureš, F.; Macak, J. M. Atomic Layer Deposition of MoSe$_2$ Using New Selenium Precursors. *FlatChem* **2020**, *21*, 100166.

(17) Charvot, J.; Zazpe, R.; Krumpolec, R.; Rodriguez-Pereira, J.; Pavliňák, D.; Pokorný, D.; Klikar, M.; Jelínková, V.; Macak, J. M.; Bureš, F. Deposition of MoSe$_2$ flakes using cyclic selenides. *RSC Adv.* **2021**, *11*, 22140−22147.

(18) Büttner, P.; Scheler, F.; Pointer, C.; Döhler, D.; Barr, M. K. S.; Koroleva, A.; Pankin, D.; Hatada, R.; Flege, S.; Manshina, A.; Young, E. R.; Mínguez-Bacho, I.; Bachmann, J. Adjusting Interfacial Chemistry and Electronic Properties of Photovoltaics Based on a Highly Pure Sb$_2$S$_3$ Absorber by Atomic Layer Deposition. *ACS Appl. Energy Mater.* **2019**, *2*, 8747−8756.

(19) Büttner, P.; Scheler, F.; Pointer, C.; Döhler, D.; Yokosawa, T.; Spiecker, E.; Boix, P. P.; Young, E. R.; Mínguez-Bacho, I.; Bachmann, J. ZnS Ultrathin Interfacial Layers for Optimizing Carrier Management in Sb$_2$S$_3$-based Photovoltaics. *ACS Appl. Mater. Interfaces* **2021**, *13*, 11861−11868.

(20) Büttner, P.; Döhler, D.; Korenko, S.; Möhrlein, S.; Bochmann, S.; Vogel, N.; Mínguez-Bacho, I.; Bachmann, J. Solid state interdigitated Sb$_2$S$_3$ based TiO$_2$ nanotube solar cells. *RSC Adv.* **2020**, *10*, 28225−28231.

(21) Schneider, C. A.; Rasband, W. S.; Eliceiri, K. W. NIH Image to ImageJ: 25 years of image analysis. *Nat. Methods* **2012**, *9*, 671−675.

(22) Stringer, C.; Wang, T.; Michaelos, M.; Pachitariu, M. Cellpose: a generalist algorithm for cellular segmentation. *Nat. Methods* **2021**, *18*, 100−106.

(23) Koch, V. M.; Barr, M. K. S.; Büttner, P.; Mínguez-Bacho, I.; Döhler, D.; Winzer, B.; Reinhardt, E.; Segets, D.; Bachmann, J. A solution-based ALD route towards (CH$_3$NH$_3$)(PbI$_3$) perovskite via lead sulfide films. *J. Mater. Chem. A* **2019**, *7*, 25112−25119.

(24) Nezu, S.; Larramona, G.; Choné, C.; Jacob, A.; Delatouche, B.; Péré, D.; Moisan, C. Light Soaking and Gas Effect on Nanocrystalline TiO$_2$/Sb$_2$S$_3$/CuSCN Photovoltaic Cells following Extremely Thin Absorber Concept. *J. Phys. Chem. C* **2010**, *114*, 6854−6859.

(25) de Paula, C.; Richey, N. E.; Zeng, L.; Bent, S. F. Mechanistic Study of Nucleation Enhancement in Atomic Layer Deposition by Pretreatment with Small Organometallic Molecules. *Chem. Mater.* **2020**, *32*, 315−325.

(26) Xu, G.; Jin, Y.; Song, J. Improvement of the Mechanical Properties by Surface Modification of ZnCl$_2$ and Polydopamine in Aramid Fiber Composites. *Appl. Sci.* **2022**, *12*, 3119.

(27) European Union. Directive 2010/78/EU of the European Parliament and of the Council. https://eur-lex.europa.eu/legal-content/EN/TXT/?uri=CELEX%3A32010L0075 (accessed Sept 05, 2022).

(28) Shiel, H.; Hutter, O. S.; Phillips, L. J.; Turkestani, M. A.; Dhanak, V. R.; Veal, T. D.; Durose, K.; Major, J. D. Chemical etching of Sb$_2$Se$_3$ solar cells: surface chemistry and back contact behaviour. *J. Phys.: Energy* **2019**, *1*, 045001.

(29) Fleck, N.; Hutter, O. S.; Phillips, L. J.; Shiel, H.; Hobson, T. D. C.; Dhanak, V. R.; Veal, T. D.; Jäckel, F.; Durose, K.; Major, J. D. How Oxygen Exposure Improves the Back Contact and Performance of Antimony Selenide Solar Cells. *ACS Appl. Mater. Interfaces* **2020**, *12*, 52595−52602.

(30) Pore, V.; Hatanpää, T.; Ritala, M.; Leskelä, M. Atomic Layer Deposition of Metal Tellurides and Selenides Using Alkylsilyl Compounds of Tellurium and Selenium. *J. Am. Chem. Soc.* **2009**, *131*, 3478−3480.

⧉ Recommended by ACS